

# Calorimeter for adsorption energies of larger molecules on single crystal surfaces

Henry M. Ajo, Hyeran Ihm, David E. Moilanen, and Charles T. Campbell

*Department of Chemistry, Box 351700, University of Washington, Seattle, Washington 98195-1700*

(Received 30 May 2004; accepted 18 July 2004; published 29 October 2004)

A calorimeter for measuring heats of adsorption of large molecules on single crystal surfaces is described. It extends previous instrumentation for single crystal adsorption calorimetry by adding the capability for measuring larger (lower vapor pressure) molecules. This is achieved using a chopped and collimated ( $\sim 4$  mm diameter) molecular beam capable of stable 100 ms pulses of low vapor pressure substances, and a line-of-sight modification of the King and Wells method for measuring their sticking probabilities at the single crystal's surface. The heat input to the single crystal due to adsorption is detected using a pyroelectric polymer ribbon pressed against the back of the single crystal, following our previous calorimeter design. Measurements of benzene adsorption on Pt(111) prove the capability to produce a highly stable beam of flux  $\sim 2 \times 10^{14}$  molecules/( $\text{cm}^2 \text{ s}$ ) and measure adsorption energies with an absolute accuracy of  $\sim 5\%$  and a pulse-to-pulse standard deviation of 2 kJ/mol. © 2004 American Institute of Physics. [DOI: 10.1063/1.1794391]

## I. INTRODUCTION

Before the advent of single crystal adsorption calorimetry (SCAC),<sup>1-3</sup> only two indirect methods of determining heats of adsorption of molecules on single crystal surfaces were available: kinetic analysis of temperature programmed desorption (TPD)<sup>4,5</sup> and analysis of equilibrium adsorption isotherms.<sup>6,7</sup> While these methods have been applied with great success, they both have the limitation that the molecule being studied must adsorb and then desorb reversibly. If the molecule partially dissociates or if the adsorbate/substrate complex changes structure before desorption, these methods cannot be used. As one might expect, the most interesting and reactive adsorbates do not adsorb and desorb reversibly, hence the need for a direct calorimetric method, namely SCAC, which measures directly the heats of adsorption of molecules on single crystal surfaces, even if they do not adsorb reversibly. If dissociation occurs upon adsorption, SCAC can provide the heats of formation of the products of the dissociative adsorption event.

Borroni-Bird *et al.* at Cambridge developed SCAC as a precise measurement technique with their paper using SCAC to measure the heat of adsorption of  $\text{O}_2$  on Ni(110).<sup>1</sup> The SCAC system constructed at Cambridge<sup>2,8</sup> includes a pulsed supersonic molecular beam, a  $\sim 0.2$   $\mu\text{m}$  thick single crystal sample, and a detector of the heat rise of the crystal based on transient infrared light detection (optical pyrometry). Its method of measuring heats of adsorption is by detection of the blackbody radiation from the back of this ultrathin single crystal due to the adsorption of the pulse of molecules. These infrared photons are collected from the back of the sample and directed through a window in the vacuum chamber onto an external infrared detector. In order to report their heats of adsorption per mole of gas adsorbed, they measured the sticking probability as a function of coverage to determine what fraction of molecules sticking the surface contribute to

the observed heat. They further showed that if the bonding of the adsorbed species produced is known as a function of coverage, one is also often able to transform these measurements into adsorbate-substrate bond energies within a pairwise bond additivity model.<sup>9,10</sup>

While Ge *et al.*,<sup>9</sup> Brown *et al.*,<sup>10,11</sup> and Kose *et al.*<sup>12,13</sup> has applied SCAC to study a large number of adsorbates on a wide variety of single crystal metals, they have only studied high vapor pressure molecules (molecules which are gases at room temperature and atmospheric pressure), like CO, NO,  $\text{O}_2$ , and ethylene.

Stuckless *et al.* has developed a similar SCAC system but with a very different heat detector<sup>3</sup> and applied it to measure heats of adsorption of metal atoms on single crystal surfaces of metals,<sup>14,15</sup> metal oxides,<sup>14-19</sup> and Si(100).<sup>20</sup> A schematic is shown in Fig. 1. We use this same type of calorimeter system here, with the main difference being in the details of producing the molecular beam. The heat of adsorption is measured by contacting a 9  $\mu\text{m}$  thick  $\beta$ -polyvinylidene fluoride (PVDF) pyroelectric ribbon to the back of the single crystal.<sup>21</sup> The use of this pyroelectric detector increases the sensitivity of the SCAC over that was developed by Borroni-Bird *et al.* thus allowing use of thicker single crystals (which have higher heat capacity) of 1 to 8  $\mu\text{m}$ . It also has improved sensitivity at low temperature compared to the Borroni-Bird *et al.* infrared detection method, where sensitivity theoretically falls by a factor of 27 from 300 to 100 K.<sup>19</sup> The ability to cool the sample promises much more flexibility in the type of adsorbate formed, since adsorption temperature greatly affects the bonding between the adsorbate and surface. A chopped effusive metal atom beam was used as the pulsed metal atomic gas source.

Here we describe a SCAC system, which is designed to measure heats of adsorption of larger, low vapor pressure molecules, using a heat detector similar to that used earlier by our group.<sup>21</sup> By "low vapor pressure molecules," here we

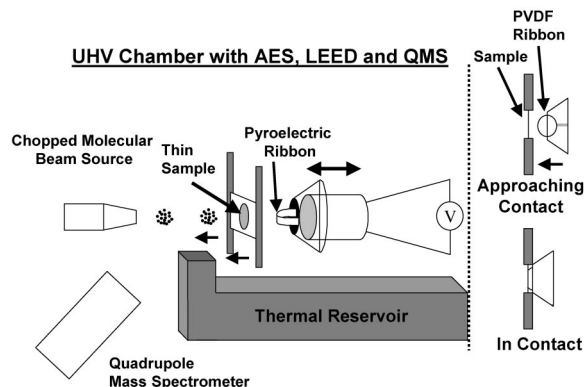


FIG. 1. Schematic of the new calorimeter. Benzene molecules from the chopped molecular beam source impinge on the  $1\ \mu\text{m}$  thick Pt(111) sample. In sticking probability measurements, the quadrupole mass spectrometer is used to determine the fraction of molecules that stick on the surface. In calorimetry measurements, the  $\beta$ -polyvinylidene fluoride (PVDF) ribbon is pressed into the back of the Pt(111) sample to make good thermal contact and then detects the temperature rise of the sample due to the heat of adsorption of the incoming molecules.

mean substances whose vapor pressures are negligible at liquid nitrogen temperature (so they can be pumped by liquid-nitrogen-cooled walls), less than  $\sim 100$  Torr at room temperature (so they cannot be formed into a molecular beam easily with a supersonic nozzle expansion), but greater than a 0.01 Torr at room temperature (so that they can be formed into a molecular beam with an effusive source operating below  $\sim 400$  K). This includes species like benzene and other larger organic molecules with molar mass exceeding  $\sim 70$  g/mol, which are *not* suitable for the type of molecular beam designs used in either of the previously reported SCAC systems, which require substances whose vapor pressures are either much higher, like CO, O<sub>2</sub>, NO, and ethylene,<sup>1,2</sup> or much lower (i.e., metal atoms).<sup>3</sup> The main difference between this calorimeter and that described previously by our group<sup>3</sup> is the use of an effusive molecular beam designed for low vapor pressure substances instead of for metal atoms.

This molecular beam must be well collimated and pulsed (100 ms pulses with a repeat period of 2 s) and compatible with the ultrahigh vacuum (UHV) chamber containing the single crystal. It must also be produced in a way that generates only low intensity vibrations of the main UHV chamber, since the pyroelectric heat detector is also a very sensitive detector of mechanical vibrations (it has a high piezoelectric coefficient). It must also be chopped into pulses in a way that causes minimal change in the infrared radiation from the beam line, which impinges on the sample and would cause spurious heat signal. These demands create some challenges, which were solved as described below. The calorimeter's pyroelectric heat detection scheme is identical to that used previously,<sup>3,21</sup> as are the electronics and computer interfacing for amplifying and storing the calorimeter detector's voltage signal versus time.<sup>3,21</sup>

As with the earlier SCACs,<sup>1-3</sup> we calibrate the heat signal for this detector by measuring the heat signal from a diffuse laser beam which is chopped and collimated before it impinges on the sample in an identical fashion to the gas beam. A method for measuring the laser power *in situ* has

been developed here, taking advantage of another pyroelectric detector made from LiTaO<sub>3</sub> (LTO), which we use with our existing electronics. Previously, LTO has been used as the detector for adsorption calorimetry.<sup>22,23</sup> Here we use it only to measure the laser intensity.

The gas flux is measured here by direct impingement of the molecular beam onto the surface of a liquid-nitrogen-cooled quartz crystal microbalance (QCM). The QCM is liquid nitrogen cooled to ensure that the sticking probability of the low vapor pressure molecules studied is unity on its surface. Their sticking probabilities on this gold-covered surface are closer to zero at room temperature. The gas flux is measured also in two more traditional ways: by direct impingement of the molecular beam into the ion source of a mass spectrometer or by measuring the mass spectrometer signal due to the background pressure rise when the beam impinges on a sample with zero sticking probability.

## II. ULTRAHIGH VACUUM (UHV) CHAMBER

The main UHV chamber is pumped routinely by a 220 l/s turbo pump (Balzers-Pfeiffer) and alternately by a 220 l/s triode ion pump (Varian). The base pressure is  $\sim 2 \times 10^{-10}$  mbar when pumped only by the turbo pump. Typically the turbo pump was kept running during calorimetry runs. A liquid nitrogen cooled titanium sublimation pump can also be used. The main chamber has two levels, with the upper level  $\sim 15$  cm above the other. A sample manipulator in the center of the chamber moves the sample between these levels, rotates the sample, and moves it onto the calorimeter's sample holder using forks that hold the sample platen just as described earlier.<sup>19</sup>

The upper level contains an energy analyzer for positively and negatively charged particles (Leybold Heraeus EA-11) and is used for characterization of the sample's surface by various techniques: Auger electron spectroscopy (AES), x-ray photoelectron spectroscopy (XPS), and low energy ion scattering spectroscopy (LEIS). The system also contains low energy electron diffraction (LEED) optics (Physical Electronics). A quadrupole mass spectrometer (QMS) (Leybold Inficon) is used to monitor the vacuum in this upper level, as well as for temperature programmed desorption (TPD) measurements with line-of-sight to the sample.

The lower level of the UHV chamber is designed for calorimetry and sticking probability measurements. It contains an electron beam for heating the sample, the calorimeter detector, a QMS (made by UTI) with a flag, a LTO heat sensor, a QCM (Leybold Inficon), and the molecular beam. The QMS in this level can be translated such that its ion source sits in the path of the molecular beam, to verify the beam's composition as well as measure its flux and pulse-to-pulse standard deviation. This QMS is also used to measure the sticking probability by translating it to intercept the molecules leaving the surface (thus measuring the fraction that do not stick — see below). Between the QMS and the sample's surface is a movable flag, which can be raised or lowered to

perform non-line-of-sight sticking probability measurements using the King and Wells method,<sup>24</sup> or a line-of-sight modification of it.<sup>3</sup>

The LTO sensor is used to measure the power of the laser beam striking the sample. This can also be done using the pyroelectric ribbon on the calorimeter detector itself. The energy deposited in these pyroelectric materials by a pulse from the chopped laser beam results in a transient face-to-face voltage change that is measured and, with the appropriate calibration, can be used to determine the average energy of the laser pulses, which is in turn used to calibrate the calorimeter's response to heat input to the single crystal sample.

The QCM can be translated just in front of the sample to intercept the molecular beam, in order to measure its flux. This QCM is cooled with liquid nitrogen to assure a sticking probability of unity for the molecular beam pulses on its gold-coated crystal face, and is used to determine the flux of the molecular beam. It is a true flux detector, as opposed to the QMS, which is a number density detector. The molecular beam is produced, and partially collimated in another vacuum chamber, which can be valved off from the main UHV chamber.

### III. SAMPLE PREPARATION

The thin Pt(111) single crystal sample used in these experiments was 1.0  $\mu\text{m}$  thick and 1.0 cm in diameter and was supplied by Jacques Chevallier at Aarhus University, Aarhus, Denmark. It was sandwiched and spot-welded between two thin (250  $\mu\text{m}$ ) tantalum sheets ( $15 \times 15 \text{ mm}^2$ ), each of which had concentric 8 mm diameter holes to leave a circular area 8 mm in diameter in the center of the sample exposed. This sample/Ta sandwich was then mounted over the 13 mm diameter hole in the 1.5-mm-thick front face of the stainless steel sample platen. After pumping down from atmosphere and baking out, the Pt(111) sample was initially covered with a carbonaceous overlayer which was sputtered away with 2.0 keV Ar ions at an Ar pressure of  $4 \times 10^{-7}$  mbar (ion source pressure =  $\sim 10^{-5}$  mbar), until LEIS revealed that Pt sites were exposed. Subsequently the sample was annealed in  $\text{O}_2$  gas at a pressure of  $1 \times 10^{-6}$  mbar for 5 min at 748–773 K. The temperature of the sample was monitored using an optical pyrometer. The chamber was then allowed to pump down for  $\sim 10$  min after which the sample was flashed to 973–1100 K. This was repeated until AES and  $\text{He}^+$  LEIS spectroscopies revealed a clean Pt(111) surface, with no carbon detected by AES. After initial sputtering, the sample was always cleaned with the oxygen anneal and flash anneal. The ultrathin Pt(111) sample appeared warped after annealing, but gave an acceptable hexagonal LEED pattern similar to that seen previously from such thin crystals.<sup>3</sup>

### IV. COLLIMATED MOLECULAR BEAM OF LOW VAPOR PRESSURE MOLECULES

#### A. Beam design and performance

The effusive molecular beam consists of two main elements: a gas handling system, and a beam line as shown in Fig. 2. The gas handling system is designed to supply a

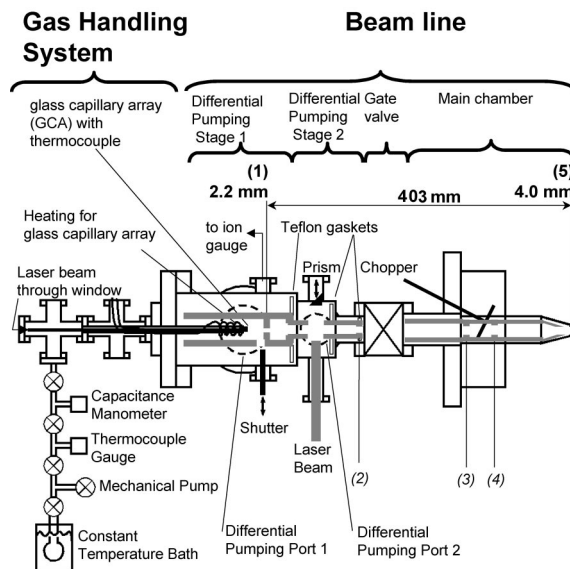


FIG. 2. Schematic of the effusive molecular beam and its separate elements: gas handling system and beam line, with five orifices indicated by numbers: (1)–(5). The beam line consists of two differential pumping stages separated from the main chamber by a gate valve. The purpose of the gas handling system is to deliver the low vapor pressure molecules in the constant temperature bath, kept at 280 K, to the glass capillary array (GCA). The temperature of the GCA is monitored by a thermocouple and is resistively heated to maintain a temperature of 300 K. The line between the constant temperature bath and the GCA is maintained at 290 K, using heating tape, to prevent condensation of the low vapor pressure molecules along the way. The beam line consists of five orifices, only two of which are beam defining: (1) and (5). The inner diameter (ID) of (1) and (5) are 2.2 and 4.0 mm, respectively, and the distance between them is 403 mm. Orifices (2), (3), and (4) which are not beam defining, but only slightly larger, have IDs of 2.8, 3.8, and 4.0 mm, respectively. Also indicated are ports for the laser and prism for calibration with the laser beam, the shutter, used to block the molecular beam, and the chopper, used to chop both the laser and molecular beams.

steady pressure of the low-vapor-pressure molecule to the beam source region just behind a glass capillary array (GCA), which directs a beam of molecules toward the sample. The source pressure can be controlled by the temperature of the reservoir and/or by partially opening a valve between the beam source and a mechanical pump. The pressure is monitored using a capacitance manometer and is usually  $\sim 5$  Torr for benzene, with the reservoir held at 280 K. The beam source and all tubulation between the reservoir and the beam source are maintained at a slightly higher temperature (290 K) than the reservoir to prevent condensation. In addition, the GCA is maintained at a still higher temperature (300 K) to prevent condensation.

The beam line consists of two differential pumping stages separated from the main chamber by a gate valve. The beam is produced at its source by passing the molecule of interest through a parallel glass capillary array (GCA). This poorly focused beam is then collimated by five other orifices, of which only the first and last define the beam diameter, while the others are slightly larger. The entire beam line, including the surroundings of the GCA, is pumped by liquid nitrogen cooled surfaces (cylindrical cryoshrouds fitted inside the outer beam-line vacuum tube walls), indicated in Fig. 2 by the gray shaded areas. In addition, the beam line is pumped by turbo pumps at differential pumping ports one

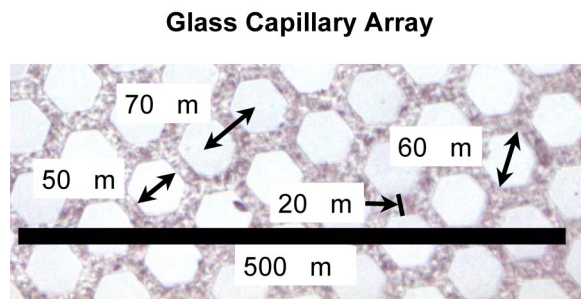


FIG. 3. Optical microscope image of glass capillary array (GCA). The GCA is an array of hexagonal close packed hexagons with their centers  $\sim 70 \mu\text{m}$  apart, with  $50 \mu\text{m}$  across the flats and  $60 \mu\text{m}$  vertex to vertex, with  $20 \mu\text{m}$  of glass separating the capillaries.

and two, as indicated in Fig. 2. The differential stages are defined by Teflon gaskets that connect (but thermally insulate) the cooled, inner surfaces from the room-temperature, outer beam-line walls. These gaskets prevent molecular flow between the first and second differential pumping stages and the main UHV chamber, except through the orifices.

The beam is initially shaped by a 1-mm-thick GCA, whose other dimensions are shown in Fig. 3. The GCA, purchased from Burle Electro-Optics (Sturbridge, MA), consists of an array of fused hexagonal tubes on a hexagonal close packed lattice, all of which are parallel to the beam line axis. Each tube in the GCA has a length to diameter ratio of 19:1, which is sufficient to ensure essentially the maximum sharpness in the angular distribution of the flux of gas it delivers, directed along its axis.<sup>25</sup> All orifices and surrounding beam line are liquid nitrogen cooled, except the GCA orifice, which along with the GCA, is in thermal contact with a heating coil to maintain its temperature at  $\sim 300 \text{ K}$  (monitored by a thermocouple, spot welded to the metal tube which holds the GCA). A thin (0.5 mm) stainless steel plate with a 2.0 mm inner diameter (ID) hole is spot welded over the GCA, leaving a 2.0 mm diameter opening for gas flow out of the GCA tubes. All the orifices between the first and last orifice are not beam defining, but are slightly larger (see Fig. 2 for sizes). These orifices are designed to enhance differential pumping down the beam line by these liquid nitrogen cooled orifices and the cylindrical cryoshrouds within each compartment between orifices. When these surfaces are cooled, these orifices effectively result in five stages of differential pumping for molecules like benzene.

The first orifice is the first beam-defining orifice, is 25.4 mm from the GCA, and has an ID of 2.2 mm. A gate valve, which isolates the beam line from the main chamber, is positioned between the second and third orifices, and a beam chopper is located between the third and fourth orifices (see Fig. 2). The final beam-defining orifice is 4.0 mm in diameter. It is 403 mm from the first defining orifice and 39 mm from the Pt(111) surface. It, and the tube that holds it (see Fig. 2), are cooled by liquid nitrogen as well.

From line-of-sight calculations, the diameter of the umbra and penumbra at the sample are 4.17 and 4.55 mm, respectively. The umbra is defined by the first and last orifices, while the penumbra is defined by the 2.0 mm diameter GCA source and the last orifice. We calculate an “effective diam-

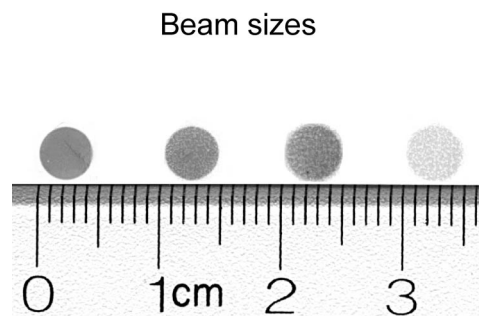


FIG. 4. These images were obtained by exposing them to white light shone down either the molecular beam path or the laser path, to estimate the sizes of the molecular beam spot size and the laser spot size, respectively. The beam sizes are shown: the two leftmost beam spots are for the molecular beam, while the two rightmost images are for the laser spot. The farthest right image is faint because of a shorter exposure time. From left to right the average diameters are 4.38, 4.33, 4.67, and 4.62 mm.

eter” of the beam by assuming unit flux inside the umbra and linearly decreasing flux to zero at the penumbra, and then finding the effective diameter of an ideal beam (with unit flux within an ideal step-function profile) needed to get the same total, area-integrated beam flux. This gives an effective diameter of 4.36 mm, nearly the average of the umbra and penumbra, as expected for these dimensions.

We measured the beam diameter by shining white light down the beam path and creating an image on photographic paper, which was subsequently developed. This gave an umbra diameter of 4.22 mm, a penumbra diameter of 4.50 mm, and an average value of 4.36 mm, as shown in Fig. 4, by averaging from the two leftmost spots. The average value matches exactly the effective beam diameter calculated above.

If one assumes that the flux in the umbra is one and the flux linearly decreases to zero at the penumbra and integrates over the area of the umbra and penumbra, one can see that the flux in the penumbra is about 10% of the total flux. As mentioned previously,<sup>3</sup> with 9% of the flux in the penumbra region, heat flow modeling shows that the penumbra contributes to about 6% of the calorimeter’s heat signal, so we expect a  $\sim 7\%$  contribution here. In this region, the surface’s adsorbate coverage does not build up as fast as within the umbra, which leads to slight inaccuracies in the relationship between measured heat and coverage.

Between the third and the fourth orifices, the molecular beam is chopped by a chopper wheel, resulting in periodic pulses at a frequency of 0.500 Hz with a duration of 100 ms. The chopper is a rotating disk mounted on the axis of a bellows-type rotational vacuum feedthrough mounted on a miniconflat flange (Thermionics). This disk has an  $18^\circ$  notch suitably sized to pass 100 ms pulses of the laser or molecular beam when rotated at 0.500 Hz. The full width at half maximum of the chopped molecular beam pulse, as measured by the QMS, was 103.5 ms, and its period was  $2000 \pm 1 \text{ ms}$ . The direct beam QMS signal increases from 0% to  $>90\%$  in 32 ms and falls from 100% intensity to  $<10\%$  in 36 ms. We used the time-integrated peak areas of the direct QMS signal of the chopped molecular beam pulses to determine that the

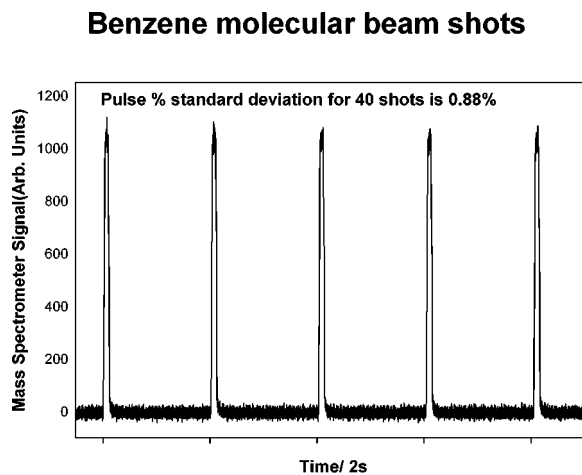


FIG. 5. Quadrupole mass spectrometer signal of five benzene shots at 0.5 Hz and of 100 ms width. The data were collected every 0.5 ms. The pulse-to-pulse relative standard deviation for these five shots plus the next 35 shots, defined as the standard deviation of the peak areas of the QMS signal for these forty pulses divided by their average, is 0.88%.

pulse to pulse standard deviation of the beam flux was 0.88%, as shown in Fig. 5.

During data acquisition, the two differential pumping stages are pumped by liquid nitrogen cooled walls and orifices as well as two 70 l/s turbo pumps (Varian). After a run, the beam is valved off from the main UHV chamber and the beam path is allowed to warm up to remove condensed molecules into these pumps. Without the molecular beam in operation, the typical base pressure read by the ion gauge attached to differential pumping stage 1, as shown in Fig. 2, is  $5 \times 10^{-9}$  mbar. With a liquid nitrogen cooling of the inside copper surfaces, it drops to  $2 \times 10^{-9}$  mbar. Starting the molecular beam by opening the valve to the gas handling system results in a pressure increase in stage 1 to  $1 \times 10^{-7}$  mbar that gradually (within  $\sim 3$  min) drops to  $4 \times 10^{-9}$  mbar with the beam running. After this period, the gate valve to the main UHV chamber can be opened. The pressure in the main chamber thereafter is barely affected by the molecular beam: the ion gauge registers small pressure bursts of  $2 \times 10^{-11}$  mbar corresponding to each pulse of the effusive molecular beam. The background pressure rise is negligible when the gate valve is opened to the flowing beam.

The typical beam flux measured for benzene at a source pressure of 5 Torr and the GCA nozzle at 303 K, running the beam at 0.5 Hz and with a pulse width of 100 ms was 0.087 ML per pulse or  $2.0 \times 10^{13}$  benzene molecules/cm<sup>2</sup> per pulse. Here, 1.00 ML is defined as the saturation coverage of benzene at 300 K, estimated to be  $2.3 \times 10^{14}$  benzenes/cm<sup>2</sup> on Pt(111) based on prior studies.<sup>26</sup> This flux allows heat measurements for 11 pulses before reaching saturation coverage, if the sticking probability is unity. Up to  $\sim 6$  Torr, the flux was proportional to the square root of the source pressure. We estimate that reasonable signal-to-noise in the calorimetry experiment could be obtained with source pressures down to  $\sim 1.0$  Torr. This would allow  $\sim 55$  pulses per ML.

It is important that the first orifice be cooled very well

with liquid nitrogen since it is irradiated with the highest flux of molecules and therefore experiences the largest heat load due to their condensation on its surface. If this orifice (or its holder) is not cold enough to ensure efficient condensation, then the pressure in the region between the source and this orifice will rise. This will also cause the gas temperature here to be colder than desired (which is equal to the warm source temperature) due to collisions of the direct beam with molecules leaving the first orifice. These two effects could result in a variety of problems. For example, we have noticed that when this orifice is not cold enough, the calorimeter signal shows that the single crystal sample is initially cooled (i.e., the heat signal goes negative) during the first 50–100 ms of each beam pulse, after which the sample is heated as expected due to the heat of adsorption. We think that this undesired initial cooling of the crystal is due to either (1) a colder optical temperature “seen” by the crystal when the room-temperature beam chopper opens, due to the high pressure of cold gas in this region, or (2) cluster formation (due to gas phase collisions in this cold region between the source and the first orifice) and subsequent, entropy-driven cluster dissociation on the warm crystal surface. Lower source pressures cure this problem, but also decrease the beam flux. High source pressures ( $>6$  Torr for benzene) make the problem appear, even when using the maximum liquid nitrogen flow allowed in our design.

## B. Calculated flux of the molecular beam

Effusive molecular beams have been used in scientific research since the beginning of the 20th century. Their properties are quite well understood and fluxes can be calculated based on the backing pressure of the molecule and the geometry of the beam.<sup>27,28</sup> Based on Refs. 27 and 28, the following equation was used to calculate the flux of our molecular beam near the centerline, where  $\tau$  is the fraction of the glass capillary array (GCA) surface that is occupied by the capillaries (0.5357),  $p_0$  is the pressure (in Torr) of the molecule in the source region behind the GCA (typically  $\sim 5$  Torr),  $M$  is the molar mass of the molecule in grams (78 for benzene),  $T$  is the temperature of the molecules ( $\sim 300$  K),  $\sigma$  is the area of the GCA (0.0314 cm<sup>2</sup>),  $j(\theta)$  is the normalized angular distribution of the beam, which is a complicated function of the dimensions of the capillaries in the GCA and the Knudsen number of the length of the capillaries, and  $\theta$  is the polar angle from the central beam axis (centerline)

$$I(\theta) = 1.125 \times 10^{22} \frac{\tau(p_0/\text{Torr})(\sigma/\text{cm}^2)j(\theta)}{\sqrt{(M/\text{amu})(T/\text{K})}} \left[ \frac{\text{molecules}}{\text{steradians second}} \right].$$

Along the centerline (i.e., at  $\theta=0$ ),  $j(\theta)$  is given by

$$j(\theta=0) = \frac{2}{3}\beta + \frac{\sqrt{\pi}}{3}\beta \frac{e^{-\delta^2}}{\delta} [1 - \text{erf } \delta].$$

Here,  $\beta$  is the ratio of the diameter to the length of the capillaries ( $\beta=2\rho/L=53.5 \mu\text{m}/1 \text{ mm}=0.0535$ ). (We approximated the hexagonal tubes as cylinders here.) The parameter  $\delta$  is a function of  $\beta$ , the Knudsen number for the

length of the capillaries ( $K_{nL}$ ), given by the mean free path ( $\Lambda$ ) of the benzene molecules in the source divided by the length of the capillaries (at  $\sim 5$  Torr,  $\Lambda/L=5.0 \mu\text{m}/1 \text{ mm}=0.0050$ ) and another function  $\alpha$ , explained below

$$\delta = \frac{\alpha}{\sqrt{2K_{nL}(1-2\alpha)}}.$$

The function  $\alpha$  given by

$$\alpha = \frac{1}{2} - \frac{1}{3\beta^2} \left( \frac{1-2\beta^3 + (2\beta^2-1)\sqrt{1+\beta^2}}{\sqrt{1+\beta^2} - \beta^2 \sinh^{-1}\left(\frac{1}{\beta}\right)} \right).$$

The preceding expression for the flux along the centerline of the beam is valid in the pressure range where  $K_{nL}$  is approximately equal to  $\beta$ .

For benzene at a source pressure of 5 Torr and temperature of 300 K, the calculated flux along the centerline is  $6.7 \times 10^{17}$  molecules/(steradian s). At the distance from the GCA to the Pt(111) surface (46.7 cm) this converts to  $3.1 \times 10^{14}$  molecules/( $\text{cm}^2 \text{ s}$ ). For the molecular beam pulse duration of 100 ms, this gives a pulse intensity at the sample of  $3.1 \times 10^{13}$  molecules/ $\text{cm}^2$  per pulse. This is somewhat larger than the measured intensity ( $2.0 \times 10^{13}$  molecules/ $\text{cm}^2$  per pulse). As noted above, the equations used are only appropriate when  $K_{nL}$  is approximately equal to  $\beta$ . However, in this case,  $K_{nL}(=0.005) < \beta(=0.0535)$ . The result is that the intensity of our molecular beam is overestimated by  $\sim 30\%$  using the preceding equation, which therefore gives an upper limit on the centerline intensity.

## V. CALORIMETER HEAT MEASUREMENTS AND CALIBRATION

Heat detection for the calorimetry measurements was done in much the same way as reported previously.<sup>3</sup> Figure 1 shows a schematic of the calorimeter. The heat detector is a  $9 \mu\text{m}$  thick, 4 mm wide, 2 cm long pyroelectric polymer ribbon, made out of  $\beta$ -polyvinylidene fluoride (PVDF) polarized perpendicular to its faces. It has a 50 nm NiAl coating on both faces to allow measuring its face-to-face voltage. This flexible PVDF ribbon can be pressed against the back of the sample to make good thermal contact with the Pt(111) sample, as is shown on the right side of Fig. 1. For calorimetry experiments, a chopped molecular beam running at 0.500 Hz with a pulse width of 100 ms is used to impinge benzene molecules on the  $1 \mu\text{m}$  thick Pt(111) sample. The heat of adsorption of the benzene molecules causes the temperature of the single crystal to rise. Since the PVDF ribbon is in good thermal contact with the sample, its temperature rises, resulting in a face-to-face voltage across the polymer ribbon. This voltage is preamplified with a fixed gain of 100, then fed to an amplifier with variable gain from 0.1–1000.<sup>3,21</sup> After this voltage is amplified, it is relayed to a computer where it is collected, displayed, and stored every 1 ms. The line shape of the resulting voltage pulses are essentially the same as those reported previously.<sup>3,21</sup> This line shape and a similar calorimeter's absolute peak intensity were well reproduced by a simulation based on system parameters such as the molecular beam's pulse duration and period, the detec-

tor's pyroelectric coefficient, the system electronics' time constants, the thermal conductivities and heat capacities of the sample, sample holder and detector components, and the sample emissivity.<sup>21</sup>

This face-to-face voltage can be converted to a heat input to the sample (in joules) for each beam pulse by multiplying by a calibration factor that we call the "ribbon/sample contact sensitivity" (in V/J). This calibration constant is measured before and after the calorimetry experiment (but during the same contact between the sample and the ribbon) using pulses of known energy imparted onto the sample with pulses from a chopped laser beam, as described previously.<sup>3</sup> The laser pulse intensity is measured during the experiment also. The reflectivity of the Pt(111) sample at this wavelength is taken from literature reports as 66%<sup>29–31</sup> when calculating the *absorbed* energy per laser pulse. The range of contact sensitivities measured on this sample was 8–40 V/J, depending on the quality of the contact, with a typical value of 10 V/J.

The laser path for such calibration is shown in Fig. 2. Light from an intensity-stable He-Ne laser (Melles-Griot,  $\pm 0.1\%$  rms over 1 min and 1 h, and  $\pm 0.2\%$  rms over 8 h) can be directed down the molecular beam path and collimated and chopped into pulses in exactly the same way as the molecular beam. It is important for this calibration that the laser and the molecular beam have the same spatial and temporal profiles. As shown in Fig. 2, this can be done in two ways. Either the laser is directed through a window behind the beam source, through the GCA, and down the entire beam path, or through a side window located downstream from the GCA and redirected down the beam path by a prism, which is driven with a manipulator into the molecular beam path when needed. The absolute laser power is measured by impinging the chopped laser beam onto either the LTO sensor or the PVDF ribbon in the UHV chamber, as described below.

The two rightmost spots in Fig. 4 are from white light shone along this latter path of the laser beam. This shows the size of the laser spot we use to calibrate the calorimeter. The average diameter of the two spots is 4.45 mm. This is  $\sim 2\%$  larger than the diameter of the molecular beam spot. For our *in situ* laser power measurements, this 2% difference is not a problem, since the laser impinges directly on the PVDF ribbon or the LTO and these pyroelectric detectors measure the net heat input and not the heat per unit area. We also estimate that this has a negligible effect on the calibration of heat pulses onto the single crystal sample since the heat input onto the sample from both the laser and the molecular beam is quickly transferred radially outward through the sample and loses its spatial definition rapidly compared to the pulse signal's rise time.<sup>21</sup>

In order to determine the contact sensitivity of our calorimeter detector, the absolute laser power at the sample must be measured. We added in this calorimeter the option of measuring this laser power *in situ* with a lithium tantalate (LTO) pyroelectric sensor in addition to direct impingement of the chopped laser beam onto the PVDF ribbon. This offers several advantages since the PVDF ribbon could lose sensitivity over time or be needed at the same time for measuring the

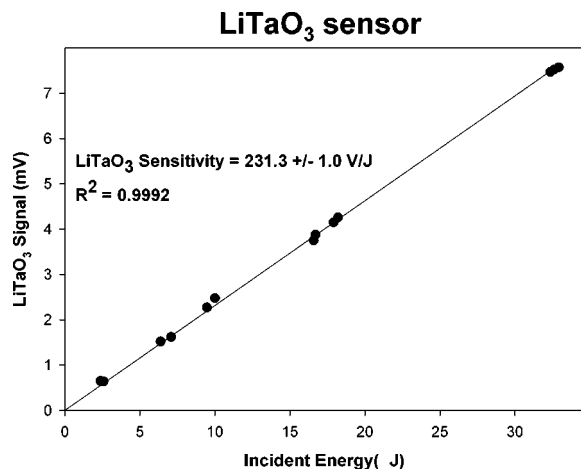


FIG. 6. The sensitivity (calibration) curve of the LiTaO<sub>3</sub> (LTO) sensor. The y axis is the original face-to-face voltage of the LTO sensor, determined by dividing the voltage after amplification (by the fixed 100 x preamplifier and the 0.1 to 1000 x variable amplifier) by the total amplification factor (a maximum of 100 000x). The x axis is the incident energy on the LTO sensor from the chopped laser beam. It is determined by multiplying the laser power (as measured in atmosphere) at the LTO by 100 ms, which is the chopped laser beam pulse width.

heat to the sample. This sensor was made by mounting a disk of polarized, optical grade LTO (Deltronic Crystal Industries, Inc., Dover, NJ), coated on both sides with gold, onto an UHV translator and attaching two contact wires for monitoring its face-to-face voltage. These contact wires were shielded and fed outside the chamber with electrical feedthroughs. The LTO sensor face-to-face voltage response to laser pulses was monitored with the same electronics as used for monitoring the PVDF ribbon's signal. The absolute sensitivity of this LTO detector was measured occasionally using laser pulses of known absolute energy. This energy was determined by measuring the absolute power of the unchopped, continuous laser beam in the same location within the UHV chamber, but after venting the chamber to atmosphere so that a calibrated photodiode detector could be inserted in the same location as the LTO sensor. This power is multiplied by the pulse duration to give the pulse energy.

Since the calorimeter detector is calibrated with laser pulses of different intensity, obtained by placing neutral density filters in the laser path, the absolute sensitivity of the LTO sensor is determined using these same filters. An example plot of face-to-face LTO voltage versus incident laser energy is shown in Fig. 6. A best-fit line through the data gives an LTO sensor sensitivity of  $231.3 \pm 1.0$  V/J. The PVDF ribbon was similarly calibrated to give a typical sensitivity of  $995 \pm 108$  V/J depending on the ribbon, assuming a reflectivity of the coated PVDF ribbon of 87%.<sup>21</sup> This allows measurement of the laser power or pulse energy during an experiment, using either the LTO sensor or the PVDF ribbon, as a backup or check. In general, the signal-to-noise ratio of this LTO detector is poorer than that of the PVDF ribbon when used to measure the identical laser pulses, presumably due to the fact that the stiffer LTO material less effectively damps out mechanical vibrations and the resulting noise due to its piezoelectric coefficient.

Since we measure the absolute beam flux and the stick-

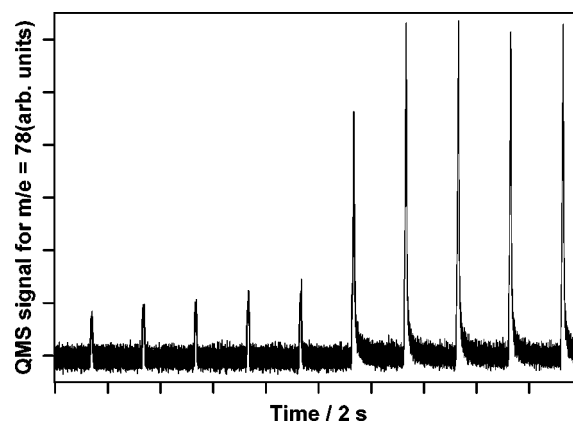


FIG. 7. Mass spectrometry signal, showing the nonsticking fraction of the molecular beam pulses before and after saturation.

ing probability as described in the following section, the heat can be converted to kilojoule per mole adsorbed. The heat of adsorption versus coverage can then be plotted and compared to the known adsorbate structure at various coverages, yielding a wealth of energetic information about the bonding of the molecule and its decomposition products to the single crystal surface.

## VI. STICKING PROBABILITY MEASUREMENTS AND BEAM FLUX MEASUREMENTS

In addition to the calorimetry measurements, we must measure the sticking probability of the benzene molecules in each gas pulse, in order to determine the fraction of benzene molecules in each pulse that contribute to the calorimetry signal. We do this by measuring the nonsticking fraction of benzene molecules with a quadrupole mass spectrometer (QMS), shown in Fig. 1.

Sticking probability measurements were done using either the famous King and Wells method,<sup>24</sup> or a line-of-sight modification of the King and Wells<sup>3</sup> method. For the latter, the translatable QMS with line of sight to the sample (but at the so-called magic angle) recorded the benzene signal while pulses of benzene hit the sample. The pulses were small and square in time initially and later became larger and grew a trailing edge in the case of benzene. The saturation of the surface by benzene was indicated by the growth of benzene signal to a constant maximum, as in Fig. 7. The sticking probability was calculated assuming that the sticking probability after saturation at 300 K is zero, a safe assumption since the multilayer desorbs more than 100 K lower in temperature.<sup>26,32,33</sup> The sticking probability for each pulse  $S_i$  was taken as unity minus the ratio of the area of the QMS signal for that pulse (i.e., the QMS signal integrated over the 2 s period of the pulse) to the area of the QMS signal at saturation

$$S_i = 1 - \frac{\text{Area of QMS signal for pulse } i}{\text{Area of QMS signal at saturation (1 ML)}} \\ = (1 - \text{QMS}_i / \text{QMS}_{\theta=1}).$$

The saturation coverage ( $N_{\text{sat}}$ ) reached after  $n$  pulses is just the sum over all  $n$  pulses of the product of (1) its beam flux

(Flux<sub>*i*</sub>) times (2) its pulse duration (100 ms) times (3) its sticking probability

$$N_{\text{sat}} = \sum_{i=1}^{i=n} [(S_i)(\text{Flux}_i)(0.1 \text{ s})] = (\text{Flux})(0.1 \text{ s}) \sum_{i=1}^{i=n} (S_i).$$

Rearranging gives

$$\text{Flux}(0.1 \text{ s}) = \frac{N_{\text{sat}}}{\sum_{i=1}^{i=n} (S_i)} = \frac{1 \text{ ML}}{\sum_{i=1}^{i=n} (S_i)}.$$

The flux can then be calculated from the sum of the measured sticking probabilities and the saturation surface coverage (if known). In the case of benzene, we have used the results of prior measurements<sup>26,32</sup> that  $N_{\text{sat}}$  (one monolayer=1.0 ML) for benzene at 300 K is  $2.3 \times 10^{14}$  benzene molecules/cm<sup>2</sup>, corresponding to one benzene for every 6.5 Pt(111) surface atoms. Using this value and the measured sticking probability for benzene, its flux was typically 0.087 ML of benzene per pulse ( $2.0 \times 10^{14}$  benzene molecules/(cm<sup>2</sup> s)), resulting in the sample being saturated by ~11 pulses at 300 K. Once the flux is known, one can calculate the coverage increment per pulse versus pulse number by multiplying the flux by the pulse duration (0.1 s) and the sticking probability for each pulse.

It is important to note that low vapor pressure molecules like benzene are often multi-atomic, so that they occupy a large area on the surface and have low saturation coverages. Thus, with the same number of molecules per pulse, one typically gets far fewer pulses per monolayer with these than when studying the much smaller molecules or atoms to which previous studies with SCAC have been limited. This tends to make data of the same absolute signal-to-noise ratio look worse since there are far fewer data points per monolayer.

One can take several different sticking probability measurements as described above at different source pressures, and thus determine the corresponding flux versus source pressure (which we found to be proportional to the square root of the pressure below 6 Torr). In this way one can also calibrate the QMS signal for the direct beam as a function of flux. Thereafter, one simply can measure the QMS signal for the direct beam to determine the flux. This was typically done as soon as possible after the calorimetry run, in case the flux should change with time.

Alternatively, one can simply determine the flux using the QCM, as it is more accurate, and does not require turning on the QMS, which causes the PVDF ribbon to be thermally disturbed from equilibrium, and thus prevents measurements of the heat signal for an undesirably long time afterward. Since one needs to measure the heat detector's contact sensitivity immediately after the calorimetry measurement, this method is most desirable. The frequency shift of the QCM that occurs when material is deposited onto it provides the mass per unit area of the deposit.<sup>34</sup> Since the sticking probabilities of benzene and similar low vapor pressure molecules are small at room temperature, flux measurements using the QCM were done with the QCM cooled to ~100 K using liquid nitrogen. At this surface temperature, the stick-

ing probability of benzene and many other low vapor pressure molecules from a room temperature source is equal to unity,<sup>33,35</sup> as required to accurately measure the flux. This was verified experimentally by the absence of a mass spectrometer signal due to these molecules in the scattering chamber while the beam impinges on the liquid nitrogen cooled QCM. Also, it is known that the molecules studied here have nearly unit sticking probabilities on their self-formed multilayers at 100 K (Refs. 33 and 35) and that their vapor pressures are negligible at 110 K, since their multilayer TPD desorption temperature peak maxima have been reported to be 180–200 K on Pt(111).<sup>26,33</sup>

The mass sensitivity of the QCM was found by depositing a known amount of metal onto the QCM at room temperature and measuring the frequency response. The absolute mass of the deposited metal was found by dissolving it into a known volume of acid solution and measuring its absolute concentration by inductively coupled plasma—atomic emission spectroscopy. The mass sensitivity of the QCM at 110 K was found to be the same as at room temperature as follows. The QCM frequency of the initial quartz crystal surface when cooled to ~100 K with liquid nitrogen ( $F_{i,\text{LN}_2}$ ) and after warming to room temperature ( $F_{i,\text{rt}}$ ) were noted, and then a multilayer palladium film was deposited on the QCM and its final frequency after metal deposition was recorded both at room temperature ( $F_{f,\text{rt}}$ ) and after recooling to ~100 K ( $F_{f,\text{LN}_2}$ ). The changes in the QCM frequency due to the metal deposition at room temperature ( $F_{f,\text{rt}} - F_{i,\text{rt}}$ ) and at liquid nitrogen temperature ( $F_{f,\text{LN}_2} - F_{i,\text{LN}_2}$ ) were compared and were found to be the same within 0.4%. After thus calibrating the mass sensitivity of the QCM, it was used while cooling with liquid nitrogen to determine the beam flux. The absolute beam flux found with this QCM agreed within experimental error with that found using the method outlined above based on sticking probabilities and known saturation coverage.

## VII. CALORIMETRIC DATA FOR BENZENE/Pt(111) AT 300 K AND COMPARISON TO OTHER METHODS

We applied this system to measure the sticking probability and heat of adsorption of benzene as a detailed function of coverage on Pt(111). The results are described in detail elsewhere,<sup>36</sup> but we summarize them here to show how the system performs. Figure 8 shows the sticking probability for benzene on Pt(111) at 300 K as a function of coverage. The initial sticking probability  $S_0$  is ~0.97, similar to values previously reported to be 1.0 at 100 K (Ref. 35) and 0.95 at 200 K.<sup>33</sup> These data are discussed in more detail elsewhere.<sup>36</sup>

We arrive at a differential heat of adsorption ( $q_{\text{ad}}$ ) from our measured heat ( $q_{\text{cal}}$ ) following:<sup>3</sup>

$$q_{\text{ad}} = -\Delta H_{\text{ad}} = q_{\text{cal}} - \left( \frac{4}{2} RT_{\text{source}} - \frac{5}{2} RT_{\text{sample}} \right),$$

where  $\Delta H_{\text{ad}}$  is the standard enthalpy change upon adsorption at the temperature of the single crystal ( $T_{\text{sample}}$ ),  $R$  is the universal gas constant, and  $T_{\text{source}}$  is the temperature of the effusive molecular beam source. If  $T_{\text{source}}$  equals  $T_{\text{sample}}$ , then the heat of adsorption is equal to the measured heat plus the kinetic energy in one degree of translational freedom

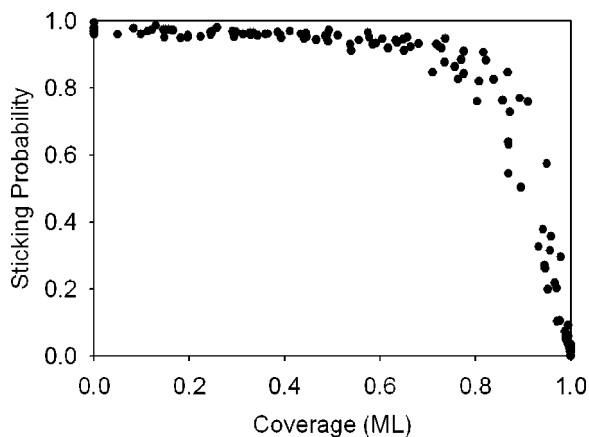


FIG. 8. Sticking probability for benzene on clean Pt(111) at 300 K. The points are from numerous different sticking probability measurements, some at different fluxes. At coverages approaching saturation, the sticking probability depends significantly on flux.

$$q_{ad} = -\Delta H_{ad} = q_{cal} + \frac{1}{2}RT.$$

The heat of adsorption as we define it here is essentially identical to the isosteric heat of adsorption<sup>9</sup> and the standard enthalpy of adsorption.<sup>3</sup>

Figure 9 shows the differential heat of adsorption (isosteric heat or standard enthalpy of adsorption) measured for benzene on Pt(111) at 300 K. As can be seen, the heat decreases nearly smoothly with coverage. These data are discussed in more detail elsewhere.<sup>36</sup> The data were well fitted by the second-order polynomial

$$(197 - 48 \cdot \theta - 83 \cdot \theta^2) \text{ kJ/mol},$$

where the coverage ( $\theta$ ) is in units of ML. The standard deviation of the data points about this curve was 1.4%, or  $\sim 2$  kJ/mol, which gives a measure of the precision of the measurement. We have achieved a similar standard deviation ( $\sim 1.8$  kJ/mol) on a Mo(100) crystal of the same thickness.<sup>37</sup> We estimate the maximum error in the absolute values of these heats as  $\sim 10\%$ , based on our uncertainties in our esti-

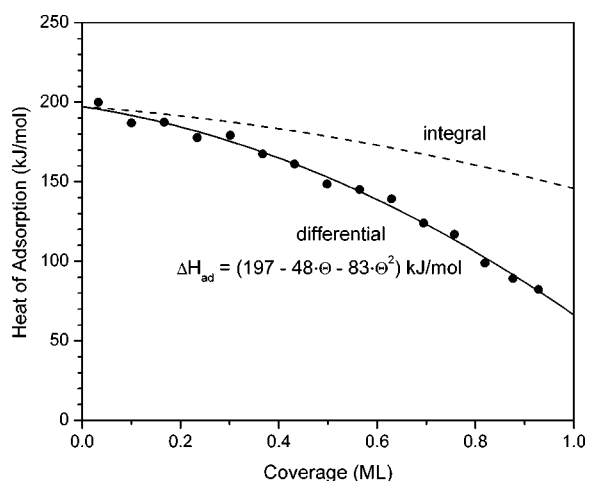


FIG. 9. Measured differential heat of adsorption of benzene as a function of coverage on Pt(111) at 300 K (dots). Also shown is the best fit to the data using a second-order polynomial dependence on coverage (solid line). The integral heat of adsorption computed using this polynomial is shown as the dashed curve.

mates of the beam flux and the optical reflectivity of our Pt(111) sample, both of which scale the data. However, there is no limitation that would prevent improving the absolute accuracy of these two measurements, so the absolute accuracy which this apparatus could routinely achieve is better than 5%.

To compare these heats of adsorption to activation barriers for desorption ( $E_a^{\text{desorb}}$ ) from TPD results, one must add  $1/2 RT_{\text{desorb}}$  to the activation barriers measured by TPD.<sup>9,38</sup> For an initial coverage of 0.8 ML, Campbell *et al.*<sup>26</sup> reported an activation energy for desorption based on TPD, assuming a prefactor of  $10^{13} \text{ s}^{-1}$  of 132 kJ/mol, which gives an adsorption energy of 133 kJ/mol. Since almost all the benzene dissociates at coverages below 0.6 ML, this value probably corresponds to an average over a range of coverages from  $\sim 0.6$  to 0.8 ML. As such, it agrees well with our calorimetry measurements. We make more detailed comparisons to experimental and theoretical results elsewhere.<sup>36</sup>

The integral heat of adsorption  $\Delta H_{\text{int}}$  is also shown in Fig. 9. It is the total heat released when adsorbing from zero coverage up to a given coverage ( $\theta$ ) and is related to our differential heat of adsorption by

$$\Delta H_{\text{int}}(\theta) = - \frac{\int_0^\theta q_{ad}(\theta) d\theta}{\int_0^\theta d\theta}.$$

These results further demonstrate the applicability of this system for direct measurements of the heat of adsorption and sticking probability of benzene on Pt(111) at 300 K. They are discussed in detail elsewhere.<sup>36</sup>

## ACKNOWLEDGEMENTS

The authors would like to acknowledge the National Science Foundation and the Department of Energy, Office of Basic Energy Sciences, Chemical Sciences Division, for support of this work. They thank Jacques Chevallier at Aarhus University in Denmark for kindly providing the single crystal. They thank Dr. J. M. Gottfried and Dr. P. Bera for collecting some of the data reported here. They acknowledge others who contributed to various aspects of this project: J. H. Larson, J. T. Ranney, D. E. Moilanen, M. Starvis, Jason Donev, Samuel Fain, and the staff of the Chemistry machine shop (B. Holm, J. Heutink, and E. McArthur) and electronics shop (J. Gladden, L. Buck, B. Beaty, and R. Olund).

<sup>1</sup> C. E. Borroni-Bird, N. AlSarraf, S. Andersson, and D. A. King, *Chem. Phys. Lett.* **183**, 516 (1991).

<sup>2</sup> C. E. Borroni-Bird and D. A. King, *Rev. Sci. Instrum.* **62**, 2177 (1991).

<sup>3</sup> J. T. Stuckless, N. A. Frei, and C. T. Campbell, *Rev. Sci. Instrum.* **69**, 2427 (1998).

<sup>4</sup> P. A. Redhead, *Vacuum* **12**, 203 (1962).

<sup>5</sup> C. M. Chan, R. Aris, and W. H. Weinberg, *Appl. Surf. Sci.* **1**, 360 (1978).

<sup>6</sup> J. Bauhofer, M. Hock, and J. Kupperts, *Surf. Sci.* **191**, 395 (1987).

<sup>7</sup> J. L. Falconer and R. J. Madix, *Surf. Sci.* **48**, 393 (1975).

<sup>8</sup> A. Stuck, C. E. Wartnaby, Y. Y. Yeo, J. T. Stuckless, N. AlSarraf, and D. A. King, *Surf. Sci.* **349**, 229 (1996).

<sup>9</sup> Q. F. Ge, R. Kose, and D. A. King, *Adv. Catal.* **45**, 207 (2000).

<sup>10</sup> W. A. Brown, R. Kose, and D. A. King, *Chem. Rev. (Washington, D.C.)* **98**, 797 (1998).

<sup>11</sup> W. A. Brown, R. Kose, and D. A. King, *Surf. Sci.* **440**, 271 (1999).

- <sup>12</sup>R. Kose, W. A. Brown, and D. A. King, Chem. Phys. Lett. **311**, 109 (1999).
- <sup>13</sup>R. Kose, W. A. Brown, and D. A. King, J. Am. Chem. Soc. **121**, 4845 (1999).
- <sup>14</sup>H. Larsen, D. E. Starr, and C. T. Campbell, J. Chem. Thermodyn. **33**, 333 (2001).
- <sup>15</sup>J. T. Stuckless, D. E. Starr, D. J. Bald, and C. T. Campbell, J. Chem. Phys. **107**, 5547 (1997).
- <sup>16</sup>C. T. Campbell, S. C. Parker, and D. E. Starr, Science **298**, 811 (2002).
- <sup>17</sup>D. E. Starr, D. J. Bald, J. E. Musgrove, J. T. Ranney, and C. T. Campbell, J. Chem. Phys. **114**, 3752 (2001).
- <sup>18</sup>D. E. Starr, S. F. Diaz, J. E. Musgrove, J. T. Ranney, D. J. Bald, L. Nelen, H. Ihm, and C. T. Campbell, Surf. Sci. **515**, 13 (2002).
- <sup>19</sup>D. E. Starr and C. T. Campbell, J. Phys. Chem. B **105**, 3776 (2001).
- <sup>20</sup>D. E. Starr, J. T. Ranney, J. H. Larsen, J. E. Musgrove, and C. T. Campbell, Phys. Rev. Lett. **87**, 106102 (2001).
- <sup>21</sup>J. T. Stuckless, N. A. Frei, and C. T. Campbell, Sens. Actuators B **62**, 13 (2000).
- <sup>22</sup>S. J. Dixonwarren, M. Kovar, C. E. Wartnaby, and D. A. King, Surf. Sci. **309**, 16 (1994).
- <sup>23</sup>R. Murdey and J. T. Stuckless, J. Am. Chem. Soc. **125**, 3995 (2003).
- <sup>24</sup>D. A. King and M. G. Wells, Surf. Sci. **29**, 454 (1972).
- <sup>25</sup>C. T. Campbell and S. M. Valone, J. Vac. Sci. Technol. A **3**, 408 (1985).
- <sup>26</sup>J. M. Campbell, S. Seimanides, and C. T. Campbell, J. Phys. Chem. **93**, 815 (1989).
- <sup>27</sup>H. Pauly, *Atom, Molecule, and Cluster Beams I*, Vol. 1 (Springer, New York, 2000).
- <sup>28</sup>H. Pauly, in *Atomic and Molecular Beam Methods*, Vol. 1, Chap. 4, edited by G. Scoles (Oxford University Press, Oxford, 1988).
- <sup>29</sup>J. H. Weaver, Phys. Rev. B **11**, 1416 (1975).
- <sup>30</sup>A. V. Sokolov, in *Optical Properties of Metals*, translated by S. Chomet, edited by O. S. Heavens (American Elsevier, New York, 1967), pp. XVII.
- <sup>31</sup>*Handbook of Optical Constants of Solids, c1998*, edited by E. D. Palik (Academic, Orlando, 1985).
- <sup>32</sup>M. C. Tsai, and E. L. Muettterties, J. Am. Chem. Soc. **104**, 2534 (1982).
- <sup>33</sup>C. Xu, Y. L. Tsai, and B. E. Koel, J. Phys. Chem. **98**, 585 (1994).
- <sup>34</sup>G. Z. Sauerbrey, Physik **155**, 206 (1959).
- <sup>35</sup>L. Q. Jiang and B. E. Koel, J. Phys. Chem. **96**, 8694 (1992).
- <sup>36</sup>H. Ihm, H. M. Ajo, and C. T. Campbell, J. Phys. Chem. B **108**, 14627 (2004).
- <sup>37</sup>J. T. Stuckless, D. E. Starr, D. J. Bald, and C. T. Campbell, Phys. Rev. B **56**, 13496 (1997).
- <sup>38</sup>J. T. Stuckless, N. Al-Sarraf, C. Cartnaby, and D. A. King, J. Chem. Phys. **99**, 1 (1993).